Broadband Signal Rather than Frequency-Specific Rhythms Underlies Prediction Error in the Primate Auditory Cortex

Andrés **Canales-Johnson**[1,2,3,*,#], Ana Filipa **Teixeira Borges**[4,#], Misako **Komatsu**[5], Naotaka **Fujii**[5],, Johannes Jacobus **Fahrenfort**[6,7], Kai Joshua **Miller**[8], Valdas **Noreika**[1,N,*]

[1] Department of Psychology, University of Cambridge, Cambridge, United Kingdom.

[2] Center for Social and Cognitive Neuroscience (CSCN), Universidad Adolfo Ibáñez, Santiago, Chile

[3] The Neuropsychology and Cognitive Neurosciences Research Center (CINPSI Neurocog), Universidad Catolica del Maule, Talca, Chile

[4] Department of Integrative Neurophysiology, Center for Neurogenomics and Cognitive Research, VU University Amsterdam, Amsterdam, The Netherlands

[5] Laboratory for Adaptive Intelligence, RIKEN Brain Science Institute, Wako, Saitama, Japan

[6] Department of Psychology, University of Amsterdam, Amsterdam, The Netherlands

[7] Department of Experimental and Applied Psychology, Vrije Universiteit, Amsterdam, The Netherlands

[8] Department of Neurosurgery, Mayo Clinic, Rochester, United States of America.

[N] Lead Contact

[#] These authors contributed equally to this work

* Correspondence: afc37@cam.ac.uk (A.C.-J.), vn261@cam.ac.uk (V.N.)

Summary

Detection of statistical irregularities, measured as a prediction error response, is fundamental to the perceptual monitoring of the environment. We studied whether prediction error response is generated by neural oscillations or asynchronous neuronal firing. Electrocorticography (ECoG) was carried out in three monkeys, who passively listened to the auditory roving oddball stimuli. Local field potentials (LFP) recorded over the auditory cortex underwent spectral principal component analysis, which decoupled broadband and rhythmic components of LFP signal. We found that broadband component generated prediction error response, whereas none of the rhythmic components encoded statistical irregularities of sounds. The broadband component displayed more stochastic, asymmetrical multifractal properties than the rhythmic components, which revealed more self-similar dynamics. We thus conclude that the prediction error response is encoded by asynchronous neuronal populations, defined by irregular dynamical states which, unlike oscillatory rhythms, appear to enable the neural representation of auditory prediction error response.

Keywords

Auditory cortex; Broadband component; Local field potentials; Mismatch negativity; Multiscale multifractal analysis; Prediction error; Rhythmic components; Scaling behaviour; Scale-free dynamics; Spectral principal component analysis

Introduction

Detection of novel sensory information enables adaptive interaction with the surrounding environment (Clark, 2013; Whitmire and Stanley, 2016). In the predictive coding framework of brain functioning, this interaction is characterized by a reciprocal loop between sensory predictions and prediction error signals (Bastos et al., 2012; Friston and Kiebel, 2009). Neural mechanisms of prediction error are typically studied by presenting a series of “standard” stimuli with intermittently occurring deviant stimuli, also called “oddballs”, and by contrasting brain responses between these stimuli categories (Chennu et al., 2013; Lumaca et al., 2019; Parras et al., 2017). This way, event-related potentials (ERP) and a range of neural oscillations have been identified as neural markers of prediction error. The most widely studied deviance ERP is the auditory mismatch negativity (MMN) – a negative deflection of electrical event-related potential recorded on the scalp or using intracranial electrodes (Halgren et al., 1995; Näätänen et al., 1978; 2007). MMN originates from the primary auditory cortex (Alain et al., 1998; Alho, 1995; Edwards et al., 2005), and it peaks around 150-200 ms in humans, whilst the peak latencies below 100 ms are typically reported in monkeys (Javitt et al., 1992; Komatsu et al., 2015). In addition to MMN, prediction error responses are observed in neural oscillations in a variety of frequency ranges including theta (3-8 Hz) (Choi et al., 2013; Fuentemilla et al., 2008; Hsiao et al., 2009; Ko et al., 2012; MacLean et al., 2014), alpha (8-12 Hz) (Ko et al., 2012; MacLean et al., 2014), beta (14-30 Hz) (Haenschel et al., 2000; MacLean et al., 2014) and gamma (>30 Hz) (Edwards et al., 2005; Eliades et al., 2014; Haenschel et al., 2000; MacLean et al., 2014; Marshall et al., 1996) ranges.

Several interpretations could be formulated aiming to explain the abundance of prediction error responses in the frequency dimension. First of all, there could be multiple independent neural mechanisms sensitive to stimulus deviance. This suggestion, however, does not explain why there would be so many distinct mechanisms with an identical functional role. Alternatively, frequency-specific detectors of prediction error might be only partially independent, forming hierarchical cross-frequency interactions. For instance, rhythms of different frequency bands could drive each other, e.g. delta phase could modulate theta amplitude and theta phase could modulate gamma amplitude in the auditory cortex (Lakatos et al., 2005). Yet another possibility – which we pursue in the present study – is that a broad frequency range of deviance responses, including theta, alpha, beta and gamma bands, points to a *broadband* prediction error response, which is not restricted to a particular frequency band, but instead is driven by an arrhythmic or asynchronous neural signal. In fact, a large number of studies reported deviance effects to run across several frequency bands (Chao et al., 2018; Haenschel et al., 2000; Hsiao et al., 2009; Ko et al., 2012; MacLean et al., 2014), arguably alluding to arrhythmic processing of unexpected stimuli.

The electrophysiological signal recorded by scalp EEG or local field potentials (LFP) is a summed activity of both postsynaptic and action potentials. Post-synaptic potentials contribute to the rhythmic oscillations of different frequency bands (Buzsaki et al., 2012), reflecting neural synchrony at specific timescales. Contrary to this, empirical data analysis and modelling suggest that the average input firing rate produces asynchronous, broadband changes across a wide frequency range (Miller et al., 2009a, 2009b; Manning et al., 2009). Such rhythmic and broadband components of LFP signal can be decomposed using spectral principal component analysis (spectral PCA) (Miller et al., 2009a, 2009b, 2017), this way separating synchronous and asynchronous neural activity. Broadband component of the LFP power spectrum is commonly characterized by a power-law function (Freeman and Zhai, 2009; He, 2014; Hermes et al., 2019), which reflects the lack of any specific temporal beat (e.g. 10 Hz) in the signal. Contrary to this, rhythmic components produce frequency-specific spectral peaks that deviate from the power law. In fact, the electrocorticography power is characterized by at least three different power-law regions of which the transitions vary across individuals and recordings in human (Chaudhuri et al., 2017; He et al., 2010) and non-human primates. The functional relevance of this heterogeneous scaling is discernible as, for instance, levels of arousal across a gradual progression from awake to grades of anaesthesia (Gifani et al., 2007) or to deep sleep (Ma et al., 2006; Weiss et al., 2009) can manifest selectively within power-law changes at different timescales. Such complex dynamics across different LFP timescales can be characterized by multiscale multifractal analysis (MMA; Gierałtowski et al., 2012), developed to analyse signal fluctuations on a wide range of timescales like those observed in LFP signals.

In the present study, we aimed to assess whether such broadband neural dynamics rather than frequency-specific rhythms underlie prediction error in the auditory cortex in the primate brain. We hypothesized that the broadband component of LFP has a multiscale scaling dynamics, distinct from that of the rhythmic LFP components.

Results

Using epidurally implanted electrodes, we recorded electrocorticograms (ECoGs) from three awake common marmosets, who passively listened to the stream of varying tones (see Fig 1A and Suppl. Fig 1A-D). By contrasting neural responses to standard and deviant tones, which were physically matched across expectancy conditions, we first identified MMN deviance response from the auditory cortex (see Fig 1B). Afterwards, we decomposed the raw LFP signal into broadband and rhythmic spectral components (following Miller et al., 2009a, 2009b, 2017; see Fig 1C). Spectral decomposition allowed us to assess whether MMN is driven by the broadband rather than oscillatory components of the LFP signal. In the following, we report a single-trial analysis that was carried out separately for

each monkey (referred to as Fr, Go and Kr), using electrodes located in the auditory cortex (see Fig 1B and Suppl. Fig 1E-H).

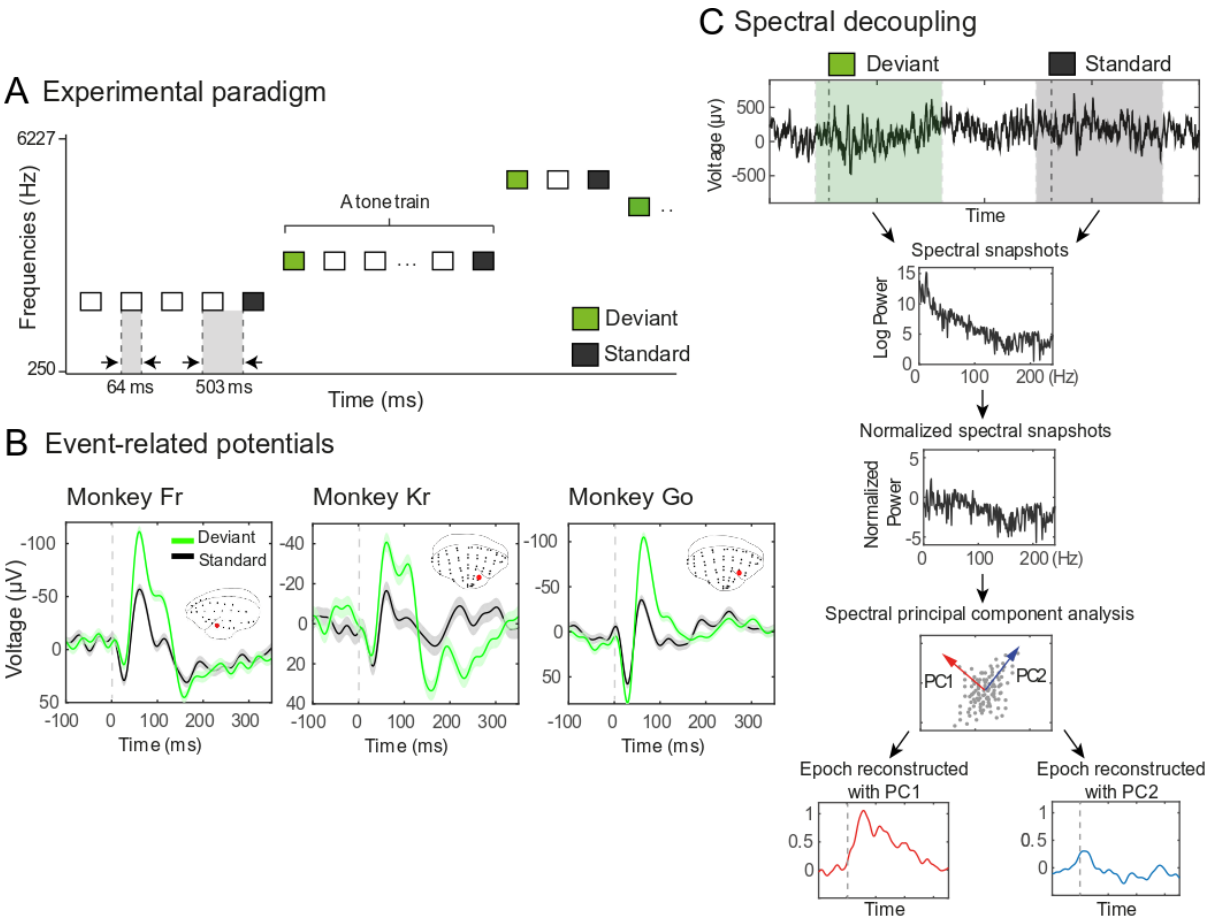

Figure 1 | Experimental design, classical ERP and spectral decoupling analysis. (A) Using a roving oddball paradigm, 20 different single-tones were presented in the trains of 3, 5 or 11 identical stimuli. Any two subsequent trains consisted of different tones. This way, while the adjacent standard (depicted in black) and deviant (depicted in green) tones deviated in the frequency due to the transition between the trains, the two expectancy conditions were physically matched, as the first and the last tones of the same train were treated as deviant and standard tones in the analysis of the adjacent stimuli pairs. **(B)** Time courses of ERP waveforms of the standard (black) and deviant (green) stimuli conditions. 0 ms time point indicates the onset of a given tone. Error shades represent the standard error of the mean (SEM), calculated across all trials at each time point. Data in this and other subplots were recorded by the electrode marked in red in the ECoG montage insets. Each subplot represents a different monkey. **(C)** Spectral decoupling. Temporally adjacent raw LFP segments of the standard tone (i.e. the last stimulus of the previous train) and the deviant tone (i.e. the first stimulus of the subsequent train) were extracted for the spectral PCA. First, Fast Fourier transform was used to calculate log power (1-250 Hz) of the raw LFP signal, which was afterwards normalized across all trials within a given expectancy condition. Normalized spectral snapshots were input into spectral PCA, which separated broadband and rhythmic components. Principal spectral components were reconstructed back to the time-series for the subsequent contrast between the expected and unexpected stimuli conditions.

Auditory ERP in the raw LFP signal

First, we confirmed that perturbation of auditory cortex with a deviant tone compared to a preceding standard tone increased the amplitude of auditory evoked potentials in the MMN time window (Fr: $t(1,719) = -7.37$, $p < 0.001$, Cohen's $d = 0.275$; Go: $t(1,1439) = -4.60$, $p < 0.001$, Cohen's $d = 0.121$; Kr: $t(1,1439) = -9.27$, $p < 0.001$, Cohen's $d = 0.244$; see Fig 1B). Latency of ERP peaks (58-66 ms) was consistent with the previous MMN studies of non-human primates (Javitt et al., 1992; Komatsu et al., 2015).

Auditory evoked responses reconstructed with broadband and rhythmic components

Aiming to differentiate broadband component of LFP signal from rhythmic sources, we carried out spectral principal component analysis that decouples the power spectrum density (PSD) into components reflecting different underlying neural dynamics (see Fig 1C and Methods). Using this technique, a broadband component can be identified by a uniform power increase, i.e. a component without clear peaks in the PSD, across a wide range of frequencies (see Fig 2A, H, O, red lines). In addition to broadband spectral changes, the technique also reveals a diverse set of narrow-band oscillatory components, revealed by peaks in the PSD (see Fig 2A, H, O, blue and black lines).

This way, three major principal spectral components (PSCs), one representing a broadband component and two representing rhythmic components, were identified from the auditory LFP signal. PSCs were highly consistent across three monkeys (see Fig 2A, H, O), matching tightly with the original depiction of spectral principal component analysis (PCA) (see Fig 1A in Miller et al., 2009b). In order to assess which of these three major PSCs encode auditory prediction error response, components were back-projected to the time dimension.

We found that the Broadband PSC carried a characteristic auditory event-related broadband (ERBB) response, reminiscent of auditory ERP, compared to largely flat responses derived from the rhythmic PSCs with alpha (Rhythmic 1) and delta (Rhythmic 2) peaks. The ERBB response was evident in the average of individual - standard and deviant - responses (see Fig 2B, I, P) as well as along the whole sequence of 11 identical tones as compared to the tone sequences reconstructed from the Rhythmic components (see Fig 2C-E,J-L,Q-S). Repeated measures ANOVA between the PSC (Broadband, Rhythmic 1, Rhythmic 2) and the stimulus expectancy (standards, deviants) factors revealed the main effects for the PSC and the stimulus expectancy, and the interaction between the PSC and the stimulus expectancy factors (see Fig 2F,M,T). Post-hoc comparisons showed that the ERBB response locked to the deviant tones had a larger amplitude compared to the ERBB response locked to the standard tones in the Broadband PSC contrast, but not in the Rhythmic 1 PSC nor the Rhythmic 2

PSC contrasts (see Fig 2G,N,U). We thus conclude that MMN response recorded by the ECoG of the auditory cortex is driven by broadband rather than rhythmic components of LFP signal.

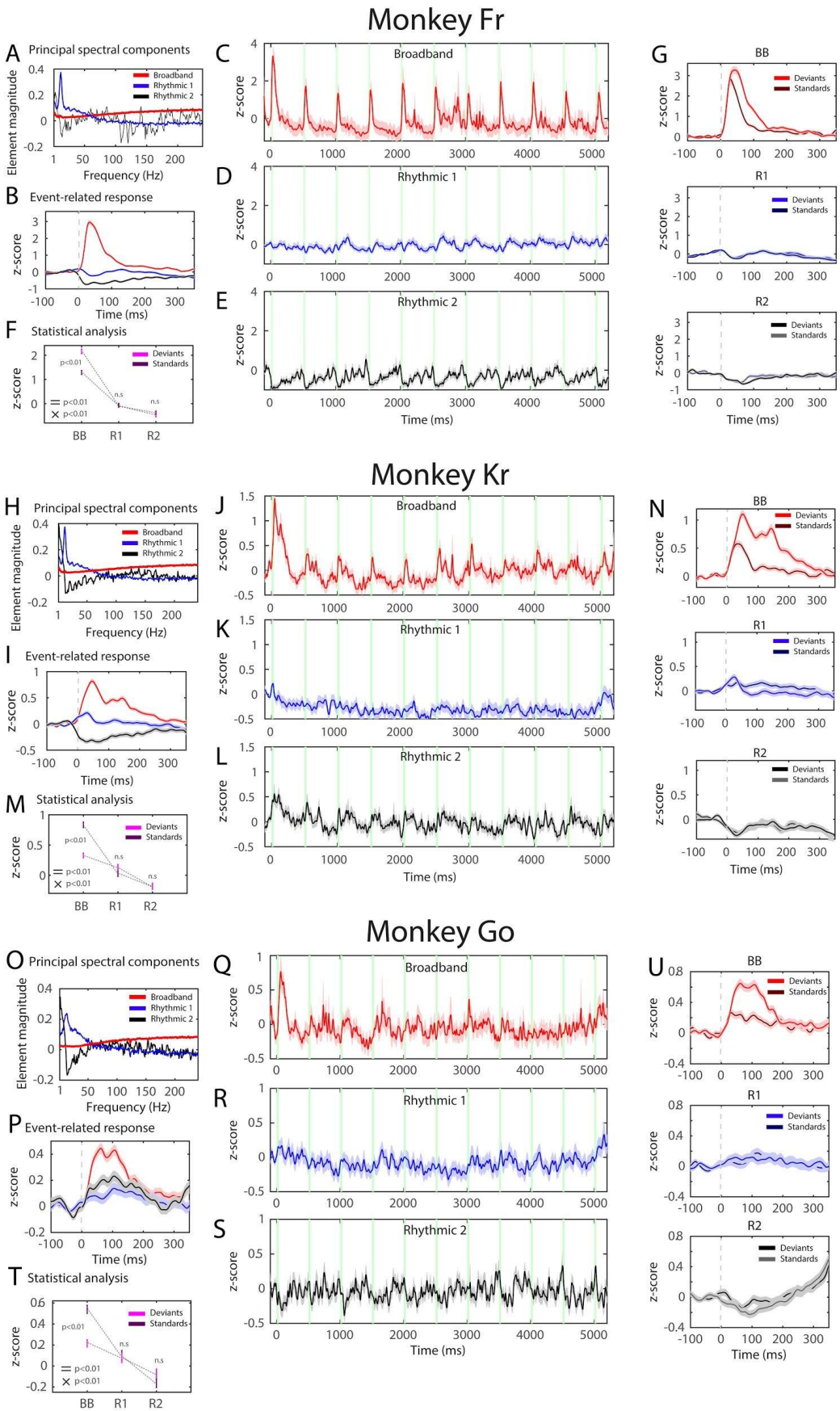

Figure 2 | Event-related broadband response of stimulus expectancy. (A,H,O) Element magnitude of the major principal spectral components (PSCs) in the frequency domain (1-240 Hz). In this and other subplots, the Broadband PSC is depicted in red, the Rhythmic 1 PSC (alpha) in blue, and the Rhythmic 2 PSC (delta/theta) in black. **(B,I,P)** A narrow window of back-reconstructed time series of the broadband and rhythmic PSCs, locked to the onset of tones (0 ms). Standard and deviant stimuli are averaged together. **(C-E,J-L,Q-S)** Back-reconstructed time series of the Broadband and Rhythmic PSCs along a sequence of 11 identical tones. 0 ms indicates the onset of the deviant tone. **(F,M,T)** ANOVA results of the stimulus expectancy (standard, deviant) and the spectral component (Broadband, Rhythmic 1, Rhythmic 2) contrast. Significant main effects were observed for the PSC (Fr: $F(2,1438)=341.70$, $p<0.001$, eta-squared = 0.322; Kr: $F(2,2878)=113.00$, $p<0.001$, eta-squared = 0.073; Go: $F(2,2878)=78.60$, $p<0.001$, eta-squared = 0.052) and the stimulus expectancy (Fr: $F(1,719)=14.1$, $p<0.001$, eta-squared = 0.01; Kr: $F(1,1439)=23.60$, $p<0.001$, eta-squared = 0.016; Go: $F(1,1439)=4.81$, $p<0.029$, eta-squared = 0.003) factors, and the interaction between the PSC and the stimulus expectancy (Fr: $F(2,1438)=17.20$, $p<0.001$, eta-squared = 0.02; Kr: $F(2,2878)=20.80$, $p<0.001$, eta-squared = 0.014; Go: $F(2,2878)=15.49$, $p<0.001$, eta-squared = 0.011). Error bars indicate the standard error of the mean (SEM). '=' refers to the main effects, 'x' refers to the interaction. **(G,N,U)** Stimuli locked waveforms show post-hoc comparisons between the standard and deviant stimuli in the broadband and rhythmic PSCs, which revealed larger amplitude for the deviant stimuli in the Broadband PSC contrast (Fr: $t=6.96$, $p_{Bc}<0.001$; Kr: $t=7.84$, $p_{Bc}<0.001$; Go: $t=5.48$, $p_{Bc}<0.001$), but not in the Rhythmic 1 (Fr: $t=0.378$, $p_{Bc}=1.00$; Kr: $t=0.612$, $p_{Bc}=1.00$; Go: $t=0.397$, $p_{Bc}=0.99$) nor the Rhythmic 2 (Fr: $t=0.812$, $p_{Bc}=1.00$; Kr: $t=-0.033$, $p_{Bc}=1.00$; Go: $t=-1.567$, $p_{Bc}=1.00$) PSC contrasts.

Cross-individual decoding of stimulus expectancy with broadband and rhythmic components

While the single-subject results of ERBB response were highly consistent across all three monkeys (see Fig 2), we wanted to establish whether the broadband prediction-error response of an individual monkey can be extrapolated to other individuals of the same species. This would indicate that the prediction error information generated in the auditory cortex is implemented similarly across monkeys. We thus assessed the cross-individual generalizability of the ERBB response by decoding the stimuli expectancy using the Broadband and Rhythmic PSCs. Using all trials of a respective PSC of one monkey, we trained a linear discriminant (LDA) classifier to learn stimuli categories (standard vs. deviant) in the auditory cortex electrode (see Fig 1B and S1). Afterwards, we decoded stimuli categories using the same PSC in a different monkey. Using Broadband PCS, we obtained significant decodability in all six pairs of comparisons, i.e. cross-individual decoding between 3 monkeys (see Fig 3A). The time windows of significant decoding above chance level (50% AUC) were consistent with MMN and BRBB responses (see Fig 1B and Fig 2G, N, U). Contrary to this, no significant cross-individual decodability was observed using Rhythmic 1 and 2 PCSs (see Fig 3B, C). These findings confirm the cross-individual generalizability of the broadband PSC encoding of stimulus expectancy.

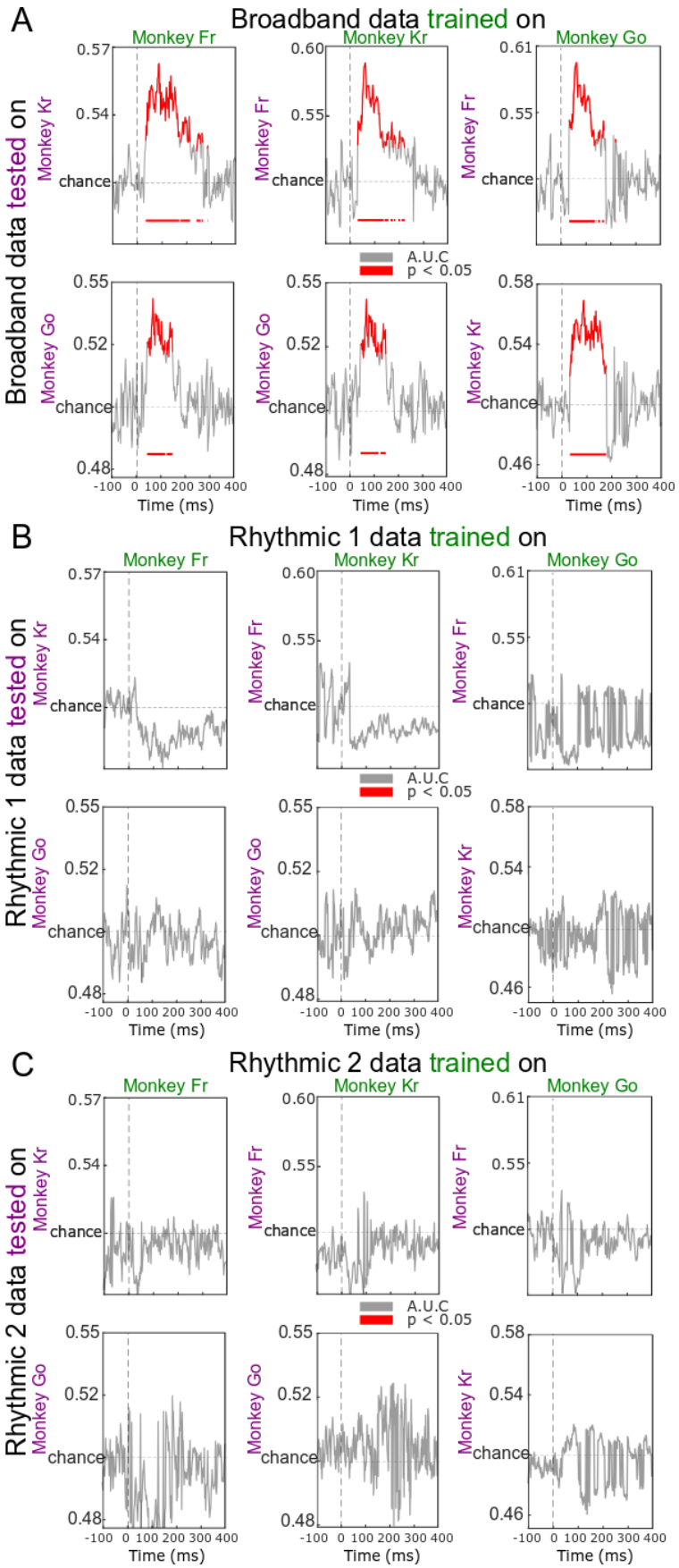

Figure 3 | Decoding of stimulus expectancy across monkeys with broadband and rhythmic components. Classification of stimulus expectancy conditions (standard, deviant) was carried out in one of the monkeys (plotted in green). Afterwards, the classifier was tested on the other two monkeys

(plotted in purple). Time points of significant decoding of stimulus categories above chance level (50% of AUC), estimated with a cluster-based permutation test, are depicted in red. **(A)** Decoding was successful in all six pairs using Broadband PSC. **(B)** Decoding did not exceed chance level using the Rhythmic 1 PSC. **(C)** Decoding did not exceed chance level using the Rhythmic 2 PSC.

Multiscale multifractal analysis of broadband and rhythmic neural components

We hypothesized that the Broadband component has a distinct multiscale temporal organization within the milliseconds of the evoked response than the one from the rhythmic components. In particular, we sought to characterize the scale-free temporal properties of the segregated neural components. These properties relate to the functional state of neural systems (Papo, 2014; He, 2014; Werner, 2010). We further hypothesized that the broadband component–-the neural signal subserving oddball detection–-has a more stochastic multiscale temporal organization which allows greater dynamical flexibility. The scale-free nature of the neuronal population firing rate, manifested in the broadband PSC (Miller, 2009; Manning et al., 2010), is usually estimated by determining the slope of the log-log function of PSD (power vs. frequency), also referred to as 1/f (fractal) scaling. However, often the PSD is not characterized by a single exponent and may show a scale-dependence (Miller, 2009; Chaudhuri et al, 2017) and/or different scaling depending on the statistical moment and hence exhibit multifractality (Nagy et al. 2017). Indeed, the single-trial auditory responses, standards and deviants, revealed a piecewise linear decay of power with frequency in each marmoset (Fig 4A), suggesting that the dynamics of the underlying processes may have scale-free properties but also a heterogeneous scaling dependent on frequency (timescale). This is noticeable by the different slopes which characterize the 1/f-like PSD depending on the frequency range (Fig. 4A), precluding the fitting of a unique line to estimate the slope across the whole spectrum. Thus, to fully characterize the scale-free properties of the three components, we sought to test for the presence of scale-dependent multifractality in the series of increments of neural activity in the marmoset auditory cortex.

Multifractality requires the presence of different scaling exponents (*h*) of different moments of the fluctuations (*q*) over a wide range of timescales (*s*) (Kantelhardt et al., 2002). Using multiscale multifractal analysis (MMA; Gierałtowski et al., 2012) (Fig 4B), which is particularly suited to analyze complex systems which exhibit fluctuations of activity on a wide range of timescales and a broad distribution of values, we found that all the three PSCs show considerable variability in the values of the generalized *q* and *s*-dependent scaling exponents (*h(q,s) – Hurst surface*) (Fig 4D). The Rhythmic components displayed similar surfaces, distinct from the nonlinear profile of *h* across $q \in [-5, 5]$ of the Broadband PSC activity. These results were consistent across monkeys (see Fig S5). The average tendency across scales revealed a nearly linear dependence of *h* with *q* for both Rhythmic components suggesting their underlying dynamics appears multifractal. Conversely, although the dynamics of the Broadband PSC is also multifractal (in the sense that its fractal properties depend on

q), the profile is nonlinear and distinct for small ($q < 0$) and large ($q > 0$) fluctuations (Fig 4E). We note that the conventional Hurst scaling analysis ($q = 2$ results) did not provide a clear distinction between the Broadband and Rhythmic 2 components. Furthermore, averaged surface values of *h* suggest the Broadband fluctuations can be quasi-stochastic ($h \sim 0.5$) or persistent without obeying strictly a power-law ($h \sim 1.1$), depending on if large ($q > 0$) or small fluctuations ($q < 0$) are considered (Fig 4F). Conversely, Rhythmic 1 and Rhythmic 2 fluctuations ranged from being close to Brownian motion (integrated white noise, $h \sim 1.5$) to scale-free. There was a qualitative agreement on the values across monkeys (Fig 4E, F). Thus, while all three PSC components showed scale-free properties, there were significant differences in the apparent stochasticity, expressed as *h(q)*, between the components (Go: RANOVA $F(2,20)=103$, $p<0.001$, eta-squared=0.339; Kr: RANOVA $F(2,20)=134$, $p<0.001$, eta-squared=0.404; Fr: RANOVA $F(2,20)=40.2$, $p<0.001$, eta-squared=0.228). For all three monkeys, the Broadband component exhibited lower *h(q)* values compared to the Rhythmic 1 (Go: $t=-14.05$, $p<0.001$; Kr: $t=-13.39$, $p<0.001$; Fr: $t=-8.54$, $p<0.001$) and Rhythmic 2 (Go: $t=-9.54$, $p<0.001$; Kr: $t=-14.88$, $p<0.001$; Fr: $t=-6.64$, $p<0.001$) components.

In order to determine whether the multifractality, depicted in the Hurst surfaces (Fig 4D), is caused by the temporal correlations of the signal distribution, we created a distribution of shuffled surrogates, i.e. copies of the original data with identical mean, variance and histogram distribution but no temporal structure. While the mean Hurst surfaces of the surrogates distribution showed for all monkeys a decrease in multifractality ($p<0.001$) (Fig 4D; Suppl. Figure 5), the averaged Hurst exponent values indicated that the neural dynamics approached randomness ($h = 0.5$) for all monkeys (Fig 4H). Therefore, the multifractality is caused mostly by the temporal correlations but also by a fat-tailed probability distribution. We subsequently computed the multifractal spectrum f(α). Analogously to a Fourier analysis, i.e. the decomposition of a signal into a sum of components with fixed frequencies, f(α) can be understood as decomposition of a signal into a set of exponents α (Mandelbrot, 2003). Their relative presence in the signal is weighted by the f(α) function. The Broadband activity interweaved more densely sets of singularities that are less self-similar than those of the Rhythmic components and displayed a lower degree of multifractality and a more asymmetrical $f(\alpha)$ (Fig 4G ,H), suggesting its dynamics differs from simple multiplicative cascades. The shape of the multifractal spectra for the Broadband activity also displayed a right-truncation (Fig 4C,G and Suppl. Figure 5), which is expected due to the leveling of *h(q,s)* for $q < 0$ (Ilhen, 2012).

To sum up, MMA analysis revealed that the generalized scale-dependent Hurst exponent *h(q,s)* and the derived *f(α)* curves of the dynamics of Broadband and Rhythmic components show multifractality as well as marked differences of this property. Importantly, the Broadband component more closely approached a stochastic asymmetrical multifractal distribution.

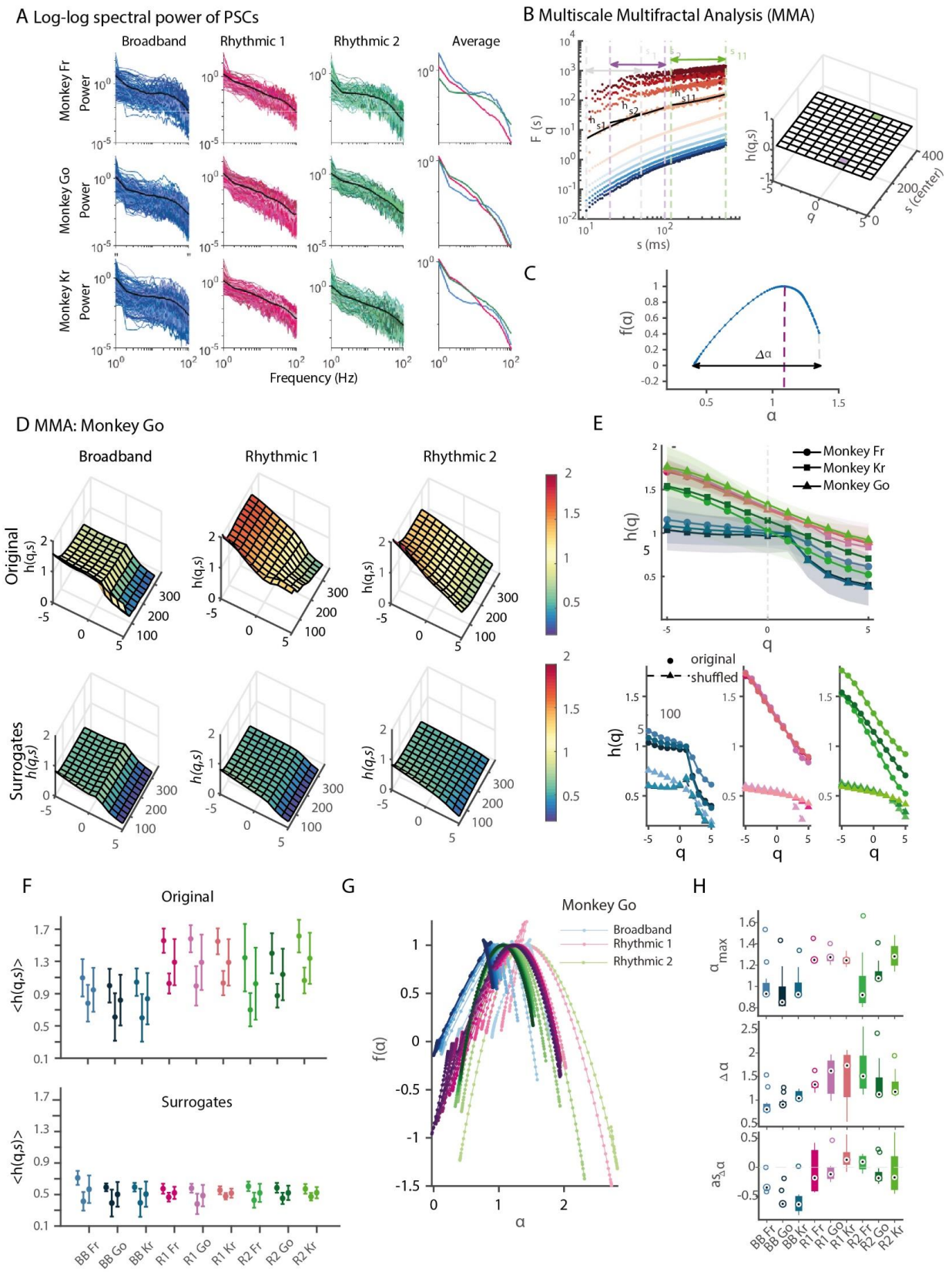

Figure 4 | Multifractal characterization of the Broadband and Rhythmic dynamics. (A) Double logarithmic plots of the power spectral densities of the Broadband (blue), Rhythmic 1 (pink) and Rhythmic 2 (green) components during all trials of the auditory MMN paradigm reveal a piecewise approximately linear decay of power with frequency. The average scaling (fractal) properties of the power spectral densities (last column) are distinct across frequencies, spectral components and

marmosets. **(B)** Multiscale Multifractal Analysis (MMA) method. *Left.* Log-log plots of the fluctuation functions $F_q(s)$ for each $q \in [-5, 5]$, color-coded from dark blue (*q* = -5) to dark red (*q* = 5) and scale *s* (in ms) of the time series correspondent to the Broadband activity of monkey Go. The Hurst (scaling) exponent ($h_{1,2,...,11}$) is obtained by determining the slope of a linear fit within a window lasting the period ($s_{1,2,...11}$) marked with vertical dashed lines. Three example scales are displayed: $s_1 \in [10, 50]$, $s_2 \in [20, 100]$ and $s_{11} \in [120, 600]$. *Right.* Computed Hurst exponents $h(q, s)$ are displayed in a (Hurst) surface plot grid. As an example, the cells corresponding to $h_{1,2,...,11}$ (*q* = 2; *s* = 1, 2 or 11) are highlighted with their respective colors (light grey, lilac, green). **(C)** The Hurst surface can also be converted into a multifractal spectrum, $f(\alpha)$, which describes how densely the singularities (i.e. scaling exponents, α) are distributed in a signal. The parabolic vertex shows the central tendency, a measure of the regularity present, and the width, the degree of multifractality ($\Delta\alpha$). **(D)** Hurst surfaces ($h(q, s)$) of the component activities (each column) and the $< h(q, s) >$ of a distribution of 50 shuffled surrogates. Monkey Go is shown here; for the other monkeys, see Figure Suppl. 5. **(E)** Scaling properties averaged for all scales. The Hurst exponent h dependency on q is evident for all components, suggesting their multifractality. **(F)** Mean (+/-SD) of the Hurst surfaces ($< h(q, s) >$) suggests that the Broadband activity has an overall more random profile. Each group of 3 dots with error bars refers respectively to $< h(q, s) >$ across all scales (s) for negative, positive and all values of q. Individual results for the Broadband (BB), Rhythmic 1 (R1) and Rhythmic 2 (R2) PSCs are displayed in variations of blue, pink and green colors, respectively. Bottom row shows the values obtained for the distribution of surrogates. **(G)** Multifractal spectrum of the three PSCs of Monkey Go, the lightness of the colors represents the results for different scales (s) (light → dark with increasing scales $s_{1,2,...11}$). **(H)** Central tendency of the multifractal spectrum (α_{max}), degree of multifractality ($\Delta\alpha$) and asymmetry of the spectrum ($as_{\Delta\alpha}$) for the three types of activity ((Broadband (BB): blue; Rhythmic 1 (R1): pink; Rhythmic 2 (R2): green)). Each monkey is displayed in a different shade of the colors.

Discussion

In the present study, we compared two alternative views of prediction error processing, namely whether LFP oscillatory vs. broadband components of neural activity encode deviant sensory stimuli. We found that auditory MMN response, a classical marker of prediction error, is primarily driven by the broadband component of LFP signal. Given that broadband PSC reflects the mean firing rate of neuronal populations (Hermes et al., 2014, 2017; Manning et al, 2009; Miller, 2010), and that neuronal spiking correlates tightly with the high-frequency LFP in the auditory cortex (Mukamel et al., 2005), our findings indicate that prediction error response depends on the asynchronous neuronal firing rate rather than oscillatory neuronal encoding of incoming stimuli.

We first replicated previous research by showing that auditory MMN is generated in the auditory cortex. Afterwards, we separated the LFP signal into Broadband and Rhythmic components and repeated MMN analyses separately for each component. While the main two rhythmic components present in the data were not able to distinguish between the standard and deviant tones, the broadband component indexed the stimuli difference in the auditory cortex. The findings were highly consistent across all three marmosets, and the cross-individual decoding successfully classified

stimuli category (standard or deviant) when data were trained on one monkey and tested on a different one. Importantly, significant decoding was observed only with the Broadband PSC, as the decoding was unsuccessful with the Rhythmic PSCs.

Our study challenges the generality of low-frequency neural oscillations as an instrument for enhancing (Schroeder and Lakatos, 2009) and gating information in the auditory cortex (Lakatos et al., 2013). In particular, it has been argued that a phase reset of slow frequencies in the range of delta and theta oscillations may underlie prediction error response (Arnal et al, 2015; Fuentemilla et al., 2008; Ko et al., 2012). However, we show that the Rhythmic 2 component with a distinctive delta peak and a considerable contribution from theta range activity (Fig 2A, H, O) does not discriminate between standard and deviant tones. Likewise, the Rhythmic 1 component representing alpha range activity did not encode prediction error response, challenging previous studies that linked MMN to alpha band power (Ko et al., 2012; MacLean et al., 2014). This contrast is striking given that these ideas were deemed most relevant in the context of rhythmic as opposed to continuous stimulation (Schroeder and Lakatos, 2009), and rhythmicity is prevalent in the current oddball paradigm. However, it is important to emphasize that we do not claim that low-frequency neuronal counterparts of neural activity do not contribute to predictive coding: long-term dependencies are relevant in sensory prediction in the auditory cortex (Rubin et al., 2016). Rather, we suggest they enable information processing through more flexible, dynamical unstable codes than an oscillatory code.

Our results demonstrate that prediction error processing is subsumed by an asynchronous broadband activity with dynamical properties very distinct from that of the rhythmic components. Importantly, this difference is unveiled when a multiscale approach is used to characterize fluctuations with several degrees of resolution (multiple fractal hierarchies) and it is patent in the surfaces and multifractal spectrum; the difference is equivocal by simply observing the power spectral densities or doing a classical Hurst analysis. The broadband component is distinctive from the other components by its lower level of self-similarity and multifractality and also by its asymmetric multifractal spectrum. The presence of multifractality in the broadband and rhythmic electrocorticographic activity suggests it may be a generic feature of neuronal networks and cognition may operate by modulations of this property (Papo, 2014). Arguably, spike trains represent information with a multifractal temporal coding (Fetterhoff et al., 2015) and the integrated multifractal spectrum permit to infer the tuning curve of spiking activity in primates (Fayyaz et al, 2019). This could be a more effective mechanism of how information is encoded in neuronal assemblies than the one provided by oscillatory rhythms. This hypothesis is bolstered by ideas that synchronization *per se* only arises in collective states where no new information can be created. In contrast, adaptive behaviour emerges from more subtle forms of coordination, e.g. through the metastability or asynchronous coupling of spatiotemporal patterns of neural activity (Friston, 2000; Tognoli and Kelso, 2014). The multifractality present in the recordings

reveals how the macroscopic neural dynamics is intermittent, its spectral density changes with time, which has been hypothesized as a facet of temporal metastability (Friston, 1997; Tognoli and Kelso, 2014); at the core of metastability is the broken symmetry of spatiotemporal patterns (Kelso and Kelso, 1995) which was only present in the broadband activity. In fact, the more asymmetrical multifractal spectra of the broadband activity suggest this feature may be a proxy of a dynamical regime which allows the breakdown of symmetry, characteristic of systems that can perceptibly or meaningfully react to afferent inputs (Freeman and Vitiello, 2006).

Furthermore, the prediction error processing by neural assemblies in the auditory cortex is sustained by an irregular broadband component with small fluctuations lying in a tight range of the non-ergodic dynamical regime $\underline{h} > 1$, which has been proposed as an explanation for the 1/*f* noise of cognitive processes (Grigolini et al., 2009), and large fluctuations with stochastic-like properties. Altogether, this result emphasizes the importance of asynchronous chaotic irregular states for optimal responsiveness to external stimuli (Beaman et al., 2017; Renart et al., 2010; Zerlaut and Destexhe, 2017).

Our findings were enabled by a novel approach to quantify these complex dynamics of neural systems, the so-called brain's "stochastic chaos" (Freeman et al., 2001). Future studies are anticipated to extend MMA analysis of MMN to wider frequency ranges (>100 Hz), with a fine-grained resolution to arguably uncover the spike tuning underlying sensory-state discrimination (Fayyaz et al., 2019). The broadband prediction error response should be further studied using hierarchical auditory prediction paradigms that can discriminate sensory and top-down prediction error responses (Bekinschtein et al., 2009; Chennu et al., 2013, 2016). Developed in human studies, such paradigms have been recently successfully applied in the common marmosets (Chao et al., 2018). Furthermore, while the marmoset model of MMN deemed successful and very stable, as indicated by cross-individual decoding, the current study should be replicated using LFP recordings in humans.

Importantly, our findings provide a unifying framework for the micro- to macro-level neural mechanisms of prediction error response. While most of the auditory MMN studies are carried out at the macro-level using scalp EEG recordings or meso-level LFP, auditory prediction error responses have also been identified using single-neuron recordings (Nieto-Diego and Malmierca, 2016; Parras et al., 2017; Pérez- González et al., 2005; Solomon and Kohn, 2014; Ulanovsky et al., 2003, 2004). In particular, individual neurons located in the primary auditory cortex increase spiking rate following presentation of oddball stimuli, which has been observed in different mammal species, including cat (Ulanovsky et al., 2003, 2004), rat and mouse (Nieto-Diego and Malmierca, 2016; Parras et al., 2017). Similar responses have also been identified in sub-cortical neurons (Parras et al., 2017; Pérez-González et al., 2005). In particular, a subclass of neurons located in the dorsal and external cortices

of the inferior colliculus of the rat respond selectively to novel auditory stimuli, while muting their response to repetitive stimuli (Pérez- González et al., 2005). A recent study of single-neuron activity recorded from different auditory centers in rats and mice suggests that prediction error response is organized hierarchically along the non-lemniscal auditory pathway comprising of inferior colliculi, medial geniculate bodies and the primary auditory cortex with sensitivity to the deviant tones increasing along the pathway (Parras et al., 2017). MMN-like deviance sensitivity of firing rate increases further in the non-primary regions of auditory cortex (Nieto-Diego and Malmierca, 2016). How do such micro-level single-neuron responses relate to the MMN potentials recorded with ECoG and/or EEG? Are different neuronal mechanisms at different levels of measurement, such as single neuron spiking rate vs. neuronal oscillations recorded using ECog/EEG?

Our study indicates that increased neuronal firing rate underlies prediction error responses not only at the micro-level of single-neuron recordings, but also at the higher meso-level LFP measurements. In particular, we show that MMN prediction error response is driven by the Broadband component of the meso-level LFP signal. Given that the Broadband PSC reflects largely stochastic neuronal firing rate, as suggested by previous modeling studies (Miller et al., 2007; Miller et al., 2009a), our findings indicate that auditory prediction error response is indeed encoded at a single action potential level within neuronal populations, which generate broadband signal at the meso- and most likely macro-level electrophysiology. Broadband LFP activity provides indirect access to the total spiking output of neurons, as shown by a growing number of experiments and simulations (Crone et al., 2011; Freeman, 2004; Rash et al., 2008). Thus, the reported Broadband activity in this study provides a ‘proxy’ for investigating the neuronal mechanisms underlying auditory prediction error. As such, the mesoscopic information of the Broadband LFP component represents a crucial link between macroscopic-level EEG and the microscopic-level spiking activity of neural populations (Buzsaki et al., 2012).

How could our LFP-based broadband results be reconciled with an abundant literature on frequency-specific MMN results, mostly derived from EEG experiments that do not find broadband MMN response across all frequencies? Miller (2010) argues that low-frequency range of broadband effects can be obscured by coincident changes in specific rhythmic phenomena. We further suggest that EEG artefacts may decrease signal-to-noise ratio in frequency-specific segments of the broadband signal, in which case only relatively clean segments would survive as significant detectors of prediction error response. For instance, blink artifacts may distort neural signal in the delta and theta frequency range (Gasser et al., 1992), whereas muscular artifacts are likely to interfere with the beta and gamma range activity (van de Velde et al., 1998). Similarly, spontaneous fluctuation of alertness level, which is likely to occur during passive “oddball” paradigms, would interfere with neural processing in the theta and alpha frequency range (Noreika et al., 2019a, 2019b). Thus, depending

on the experimental demands, the selection and training of participants, and the data preprocessing steps, certain segments of the broadband signal may be occluded by artifactual or irrelevant signals when contrasting standard and novel stimuli, yielding frequency-specific deviance responses that in fact originate from scale-free broadband component of neuronal signal. The suggested role of EEG artifacts in the preclusion of broadband response could be tested using simultaneous EEG and LFP recordings. Alternatively, too often classical frequency bands are loosely equated to specific rhythms (Lopes da Silva, 2013) and the views of collective neural network activity as oscillations lend too much emphasis on “rhythmicity” (Cole and Voytek, 2017) when in reality, in those narrow-band analyses perhaps no characteristic frequency oscillation was present and/or may even be spurious and caused by filtering (de Cheveigné and Nelken, 2017).

To conclude, we show that in a well-studied paradigm of auditory prediction error, oscillations do not constitute a means to temporally constrain information processing. They are perhaps the tips of the iceberg, the latter being an arrhythmic broadband component with asymmetric multifractal stochastic properties at several timescales. Our paper establishes the relevance of the broadband activity to encode relatively low-level auditory patterns and provides a theoretical background and empirical tools to probe which predictive values lie under the “noisy” surface in other paradigms and sensory modalities.

Methods

Subjects

We used three adult male common marmosets (*Callithrix jacchus*) that weighed 320–380 g. Monkeys were implanted with ECoG electrode array under general anaesthesia, and all efforts were made to minimize suffering. All surgical and experimental procedures were performed in accordance with the National Institutes of Health Guidelines for the Care and Use of Laboratory Animals and approved by the RIKEN Ethical Committee (No. H26-2-202). ERP data of one monkey (Fr) was reported previously (Komatsu et al., 2015), whereas datasets of monkeys Go and Kr are new.

Implantation of ECoG arrays

Chronically implanted, customized multichannel ECoG electrode arrays (Fig. S1) (Cir-Tech Inc., Japan) were used for neural recordings (Komatsu et al., 2015; 2017). We implanted 32 (the left hemisphere of monkey Fr), 64 (the right hemisphere of monkey Go), and 62 (the right hemisphere of monkey Kr) electrodes in the epidural space. For 32 electrode array, each electrode contact was 1mm

in diameter and had an inter-electrode distance of 2.5–5.0 mm (Komatsu et al., 2015). For 64 electrode array, each electrode contact was 0.6mm in diameter and had an inter-electrode distance of 1.4mm in a bipolar pair (Komatsu et al., 2017). The electrode-array covered the frontal, parietal, temporal, and occipital lobes. The additional 4 electrodes of monkey Fr covered part of the right frontal lobe. The animals were initially sedated with butorphanol (0.2 mg/kg i.m.), and surgical anaesthesia was achieved with ketamine (30 mg/kg i.m.) and medetomidine (350 µg/kg i.m.). The animals were then positioned in a stereotaxic frame (Narishige, Japan) and placed on a heating pad during surgery. Vital signs were monitored throughout surgery. Implantation of the electrode-arrays involved the removal of a bone flap (~2 cm along the anterior-posterior axis and ~1 cm along the mediolateral axis) over the parietal cortex. The array was advanced into the epidural space. After positioning the electrode-array, connectors were attached to the bone using dental acrylic and titanium (size 1.0 x 0.1mm) or PEEK (size 1.4 x 2.5 mm) screws. The reference electrodes were placed in the epidural space and the ground electrodes in the episkull space. The anti-inflammatory corticosteroid dexamethasone (1.25mg/kg, i.m.) was administered after surgery to prevent brain swelling. The animals were given antibiotics and analgesics daily for 5 days after surgery. Following the animals' recovery, the position of each electrode in the arrays was identified based on computer tomography, and then co-registered to a template T1-weighted anatomical magnetic resonance image (MRI) (http://brainatlas.brain.riken.jp/marmoset/; Hikishima et al., 2011) (monkey Fr) or pre-acquired MRI (monkeys Go and Kr) using MRIcron software (http://www.mricro.com; Rorden et al., 2007). In all monkeys, the electrode-array covered the frontal, parietal, occipital, and temporal cortices, including the primary auditory area (Fig. 2A-C and S2).

Stimuli and task

We adopted a roving oddball paradigm (Cowan et al., 1993; Haenschel et al., 2005; Garrido et al., 2008). The trains of 3, 5, or 11 repetitive single-tones of 20 different frequencies (250–6727 Hz with intervals of 1/4 octave) were pseudo-randomly presented. Tones were identical within each tone-train, but differed between tone-trains. Because tone-trains followed on from one another continuously, the first tone of a train was considered to be an unexpected deviant tone, because it was of a different frequency from that of the preceding train. The final tone was considered to be an expected standard tone, because it was preceded by several repetitions of this same tone. To avoid analytical artefacts stemming from differences in the number of standard and deviant stimuli, we considered only the last tone of a train as standard. Standards and deviants were presented 240 times in a single recording session. Pure sinusoidal tones lasted 64 ms (7 ms rise/fall), and stimulus onset asynchrony was 503 ms. Stimulus presentation was controlled by MATLAB (MathWorks Inc., Natick, MA, USA) using the Psychophysics Toolbox extensions (Pelli, 1997; Brainard and Vision, 1997). Tones were presented

through two audio speakers (Fostex, Japan) with an average intensity of 60 dB SPL around the animal's ear.

ECoG recording and preprocessing

ECoG recordings were taken in the passive listening condition while monkeys were awake. In each recording session, the monkey Fr was held in a drawstring pouch, which was stabilized in a dark room, and the monkeys Go and Kr sat on a primate chair in a dimly lit room. The length of a single session was about 15 min: the first 3 min of data were used for many standard stimuli (data are not shown in this paper) and the remaining 12 min of data were used for the roving oddball sequences. For monkey Fr, data from 3 sessions were used for analysis, which resulted in 720 (=240 × 3) standard and deviant presentations. For monkeys Go and Kr, data from 6 sessions were used for analysis, which resulted in 1440 (=240 × 6) standard and deviant presentations.

ECoG signals were recorded at a sampling rate of 1 kHz per channel. In the signal preprocessing, those signals were re-referenced using an average reference montage, and high-pass filtered above 1 Hz. We segmented datasets from −903 to 400 ms relative to the onset of the unexpected tone, so that each segment would include a pair of a deviant and a standard immediately preceding the deviant, as well as a baseline of 400 ms preceding the standard tone. The segments were then divided into standard epochs and deviant epochs (-400 ms to 400 ms). Parts of the dataset are shared in the public server Neurotycho.org (http://neurotycho.org/; Nagasaka et al., 2011).

ECoG electrode-of-interested was identified functionally by contrasting time-frequency charts between standard and deviant stimuli (0-350 ms), separately for each electrode (see Suppl. Fig. 2-4). The Hilbert transform was applied every 10 Hz and z-scored with respect to the baseline period (-100 ms to 0 ms). One electrode with the largest high-gamma difference between the standard and deviant tones (Edwards et al., 2005; Eliades et al., 2014; Haenschel et al., 2000; MacLean et al., 2014; Marshall et al., 1996) was selected for each monkey for further analyses. In all three monkeys, the selected electrode-of-interest was located in the auditory cortex (see Suppl. Fig. 1E-H).

Event-related potentials

For ERP analysis of the raw signal, a low-pass filter of 40 Hz was used. ECoG recordings were re-referenced with respect to the common average reference across all electrodes. Data were then epoched around the onset of tones (-100 ms to 350 ms), and baseline correction was applied by subtracting the mean of the 100 ms period before the stimulus onset. MMN was assessed by comparing the standard ERP and deviant ERP.

Decoupling the cortical spectrum to isolate Broadband and Rhythmic spectral components

To extract the course of broadband spectral activity, we carried out the spectral decoupling of raw LFP signal (Miller et al. 2009a, 2009b, 2017). As for the ERP analysis, ECoG potentials were re-referenced with respect to the common average reference across all electrodes. For the selected electrodes-of-interest (see above), discrete samples of power spectral density (PSD) were calculated using -200 to 400 ms epochs centered at the stimuli onset. With trials from both conditions (standards and deviants) grouped together, individual PSDs were normalized with an element-wise division by the average power at each frequency, and the obtained values were log-transformed. An inner product matrix of these normalized PSDs was diagonalized with a singular value decomposition, and was then applied to identify components of stimulus-related changes in the PSD. The eigenvectors (Principal Spectral Components or PSCs) from this decomposition revealed distinct components of cortical processing. Continuous time-frequency power charts were calculated using complex Morlet wavelets. These power charts were then normalized in the same way as the discrete spectra and projected onto the first PSC (broadband), second PSC (alpha rhythm, ~ 10 Hz), and third PSC (delta rhythm, ~2 Hz), separately. The raw time series were smoothed with an 80-ms Gaussian envelope (SD 80 ms), *z*-scored per trial, using a pre-stimulus period between -100 to 0 ms, and exponentiated, and then a value of 1 was subtracted (setting the mean at 0). The first PSC allowed to obtain the "broadband time course" which has been shown to reflect a power law in the cortical PSD (Miller et al., 2009a), and the second and third PSCs uncovered the "rhythmic time courses" with distinct frequency peaks.

Cross-individual decoding

To assess cross-individual generalizability of our findings, a univariate temporal decoding model was applied on each individual PSC time-courses on the selected auditory cortex electrodes, aiming to decode the stimuli expectancy categories, i.e. standards vs deviants. (Figure 3). The ADAM-toolbox was used on the Broadband and Rhythmic PSC time-courses with epochs from -100 ms to 400 ms (Fahrenfort et al., 2018). Crucially, and for each individual component, we trained a linear discriminant (LDA) classifier in one monkey and tested in a separate monkey for obtaining cross-individual decodability of stimuli expectancy category, i.e. standard vs deviant trials. As decoding algorithms are known to be time-consuming, data were downsampled to 250 Hz. Next, a backward decoding algorithm, using either stimulus expectancy category was applied according to a tenfold cross-validation scheme. A linear discriminant analysis (LDA) was used to discriminate between stimulus classes (e.g. deviant versus standard trials) after which classification accuracy was computed as the area under the curve (AUC), a measure derived from the Signal Detection Theory. AUC scores were tested per time-point with double-sided t-tests per subjects against a 50% chance-level. These t-tests

were corrected for multiple comparisons over time, using cluster-based permutation tests ($p<0.05$, 1000 iterations). This procedure yields time clusters of significantly above-chance classifier accuracy.

Dynamical characterization of the scaling behaviour

To characterize the scaling properties of the neural activities of all PSCs of all monkeys, we combined all individual trials for each PSC after removing their baseline – the resulting series had a length of 1327920 (Monkey Fr) and 2655840 samples (Monkeys Kr and Go) – and quantified the relationship between ln(power) and ln(frequency).

Continuous power spectral densities. The power spectral density (band: 1–100 Hz) of each combined time series for the principal components studied was computed by applying the modified Welch periodogram method as implemented in Matlab's *pwelch()* function. We used 50% overlapping Hann windows of 1.024 s.

Multiscale Multifractal Analysis (MMA). The nonstationarity of neural dynamics (Paluš, 1996) and, in particular, the existence of changing points (crossovers) in the scaling laws in the marmoset electrocorticographic data, which vary across individual and PSCs, precluded a pre-defined selection of the scales of interest and called for a data-driven scaling analysis robust to nonstationarity. Thus, to characterize the scaling behaviour, we used a method designated Multiscale Multifractal Analysis (MMA) (Gierałtowski et al., 2012). MMA is an extension of the Detrended Fluctuation Analysis (DFA) (Peng *et al.*, 1995), an established method to quantify the monofractal scaling behaviour of nonstationary signals, robust to some extrinsic trends (Hu *et al.*, 2001). DFA is essentially a modified root mean square (RMS) analysis of a random walk (Peng *et al.*, 1995). Briefly, for a given time series x_k of length N, the profile $y(k)$ is determined by integrating the time series, then $y(k)$ is split into non-overlapping segments with length s which are detrended by subtracting the local least-squares line fit, $y_s(k)$. Since N/s is often not an integer, to avoid discarding data samples, a second splitting is performed starting from the end of the time series; a total of $2N$ segments are considered. The root-mean-square fluctuation of integrated and detrended time series is given by:

$$F(s) = \sqrt{\frac{1}{2N}\sum_{k=1}^{2N}[y(k) - y_s(k)]^2}$$

A generalized version of this method—the Multifractal Detrended Fluctuation Analysis (MF-DFA) (Kantelhardt *et al.*, 2002)—permits to further characterize the fluctuations by inspecting simultaneously small and large fluctuations q dependent on the multifractal parameter :

$$F_q(s) \equiv \left\{ \frac{1}{2N_s} \sum_{k=1}^{2N} [y(k) - y_s(k)]^{\frac{q}{2}} \right\}^{\frac{1}{q}}$$

The conventional DFA corresponds to the situation in which $q = 2$, and it is for stationary random processes equivalent to the Hurst exponent (Hurst, 1951). The process is repeated for several lengths of s; typically, $F_q(s)$ increases with s and displays the asymptotic behaviour $F(s) \sim n^{h(q)}$. The generalized Hurst exponent ($h(q)$) is estimated by extracting the slope of a linear least-square regression of $F_q(s)$ on a log-log plot for a given set of s values. The MMA algorithm's advantage is that instead of prefixing a unique range of scales to estimate the scaling behaviour, it allows to scan for several scale-ranges yielding a quasi-continuous characterization of the scaling behaviour ($h(q)$), which may vary along scales (frequencies of the power spectrum): the result is a scaling exponent depending on both *q* and *s*—$h(q, s)$. It can be visualized in a grid, the Hurst surface, each cell of which corresponds to a value of *q* and a given range of scales *s*.

We applied MMA to the PSCs of the 3 marmosets within a range of $q \in [-5, 5]$ and fixed the lower scale limit to 10 samples and the upper to 600, the first being the minimum required to avoid arithmetic underflow (Gierałtowski et al., 2012), and the second to not include scales above the length of a single continuous trial. We computed MMA along 12 scales, comprising the range $s \in [10, 600]$ ms which is equivalent to ~1.67-100 Hz. The first scale integrated the scales $s_1 \in [10, 50]$ (20-100 Hz) and for $s_{2,3,\ldots,12}$ this window was progressively slid 10 ms and expanded ($s_2 \in [20, 100]$, $s_3 \in [30, 150]$ and so forth). This permitted a nearly continuous coverage of the whole spectrum, allowing to identify any crossover areas. For the detrending, we used a polynomial of order 2.

The values of $h(q, s)$ are interpreted in the following way (Gierałtowski et al., 2012): if $h(q, s) = 0.5$ the signal is constituted by uncorrelated randomness (white noise), $h(q, s) \in]0.5, 1]$ indicates persistent long-range correlations and scale-free properties, if $h(q, s) \in [0, 0.5[$ the signal has anti-correlations, $h(q, s) = 1.5$ indicates Brownian motion (integrated white noise) and, finally, $h(q, s) > 2$ indicates black noise. Further, monofractal signals will have identical h for all q values while multifractal time series display different exponent values depending on whether q is negative (short fluctuations) or positive (large fluctuations) (Kantelhardt et al., 2002). Within the regime of persistent long-range correlations, there is also a straightforward correspondence between *h* and the spectral exponent β obtained from the slope of the power spectral density ($S(f) \sim \frac{1}{\beta}$, where *f* is the frequency); according to the Wiener-Khintchine theorem: $\beta = 2h - 1$. A full description of MMA is available at (Gierałtowski et al., 2012) and we used the original code available at Physionet, (https://physionet.org/physiotools/mma/; (Goldberger et al., 2000)).

Multifractal spectrum. A complementary way of identifying the scaling properties of the different PCSs is to consider their singularities characterized by the parameters α (Lipschitz-Hölder exponent) and $f(\alpha)$, respectively associated with the strength of the singularities and how densely they are distributed (Halsey et al., 1986). Thus, the multifractal (or singularity) spectrum is described by the possible range of α values and the function $f(\alpha)$. There is an established connection between these latter measures and the exponents obtained with MMA through the known relationship between MF-DFA and the general multifractal formalism (Kantelhardt et al., 2002; Kantelhardt, 2011). Using fractal geometry and specifically the box-counting method, one can obtain an estimate of dimension by relating a linear distance (*s*) to the mass of a given object. If in an *E*-dimensional space of the observations is partitioned into (hyper-)cubes with side *s*, and one counts the number *N(s)* of cubes that contain at least one point of a set *S*, one obtains a very crude measure of this set (Feder, 1988) without any information from its structure. A better estimate applies a weighted sum that takes into consideration the number of points in each hyper-cube. For a set *S* consisting of *N* points, N_i will be the number of points in each partition *i* and the mass or probability $\mu_i = \frac{N_i}{N}$. It follows that the weighted number of boxes, N (q,s) is defined by:

$$N(q,s) = \sum i(\mu_i)^q \sim s^{-\tau(q)}$$

Where *q* is the moment order and $\tau(q)$ is the mass exponent and $\tau(0) = D_0$ is the fractal dimension of the set. If there is a linear dependency of $\tau(q)$ with *q* then, a set is monofractal, otherwise, it is multifractal. In (Kantelhardt et al., 2002), it was derived how the mass exponent relates to the *h(q)* of the method used in this report:

$$\tau(q) = qh(q) - 1$$

It follows that $f(\alpha)$ is derived from $\tau(q)$ via a Legendre transform (Halsey et al., 1986):

$$\alpha = \frac{\mathrm{d}\tau(q)}{\mathrm{d}q}$$

$$f(\alpha) = q\alpha - \tau(q)$$

Then by simply replacing Eq. 4 and 5 in Eq. 6, one obtains the singularities strength (α) and the dimensions of the subset of the time series that is characterized by those singularities ($f(\alpha)$):

$$\alpha = h(q) - qh'(q) \text{ and } f(\alpha) = q[\alpha - h(q)] + 1$$

The function $f(\alpha)$ is always convex upward and its left-hand branch corresponds to *q* > 0 and the right-hand branch to *q* <0 (Theiler, 1990). Furthermore, the central tendency (peak α_0) of the multifractal spectrum is closely related to the Hurst exponent derived from the monofractal (*q* = 2) DFA, thus representing the average fractal structure in the signal. The multifractal spectrum width ($\Delta(\alpha)$) indicates the deviation from monofractality, or conversely, the degree of multifractality (Ihlen, 2012). The ($\Delta(\alpha)$) is defined as the difference between the maximum (α_{max}) and minimum (α_{min}) values of the Lipschitz-Hölder exponent:

$$\Delta\alpha = \alpha_{max} - \alpha_{min}$$

Of note,$f(\alpha)$ is not forcefully a symmetric function and can differ from the shape like the symbol $\cap$ characteristic of the most trivial multifractals, which are not strictly self-similar (scale-free), but have a multiplicative rescaling structure, i.e. a scale-dependent self-similarity (Riedi, 1999). Therefore, we also computed a rough estimate of the degree of asymmetry:

$$as_{\Delta\alpha} = \frac{\alpha_{max} - \alpha_0}{\alpha_0 - \alpha_{min}}$$

We computed these parameters of the multifractal spectrum for all scales (*s*) analyzed with MMA and for all PCS activities of the marmosets.

Surrogate data. We created 50 shuffled surrogates by randomly permuting in temporal order the samples of the original time series of each marmoset's PSCs. If the shuffling procedure yields time series exhibiting simple random behaviour ($h = 0.5$), one can conclude that the multifractality present is due to different long-range correlations of small and large fluctuations (Kantelhardt et al., 2002). On the contrary, if shuffling does not affect the values of $h(q, s)$, the multifractality originates in a broad probability density function (PDF) of the values in the time series. If the multifractality originates both from correlations and broad PDF, the shuffling version will display weaker multifractality than the original one. All analyses were carried out in Matlab® (v. 2018a, The MathWorks).

Statistics

For ERP MMN (Fig 1) pairwise comparisons were used by comparing a pair of adjacent standard (i.e. the last tone of the N train) and deviant (i.e. the first tone of the N+1 train) stimuli. Similarly, for the spectrally-decoupled time series (Fig 2F,M,T), we performed separate repeated-measures ANOVA (RANOVA) for each individual monkey between PSC (Broadband, Rhythmic 1, Rhythmic 2) and stimulus (standards, deviants), *using* Bonferroni correction for *post hoc* comparisons. Similarly, in the case of the MMA analyses (Fig 4F), Hurst exponents were compared using RANOVA for each monkey

between PSC (Broadband, Rhythmic 1 and Rhythmic 2) and *post hoc* comparisons were Bonferroni corrected. Statistical analyses were performed using open-source statistical software *jamovi* (Version 0.9; Jamovi project, 2019).

Acknowledgments

We thank Robin Ince, Laura Imperatori and Daniel Bor for contributing to valuable discussion. This manuscript is dedicated to the memory of Prof. Walter J. Freeman (1927 - 2016) whose pioneering work on Neurodynamics has inspired countless meaningful insights during the execution of this project.

References

Alain, C., Woods, D. L., and Knight, R. T. (1998). A distributed cortical network for auditory sensory memory in humans. Brain Research *812*, 23-37.

Alho, K. (1995). Cerebral generators of mismatch negativity (MMN) and its magnetic counterpart (MMNm) elicited by sound changes. Ear and Hearing *16*, 38-51.

Arnal, L.H., Doelling, K.B., and Poeppel, D. (2015). Delta-beta coupled oscillations underlie temporal prediction accuracy. Cerebral Cortex *25*, 3077–3085.

Bastos, A. M., Usrey, W. M., Adams, R. A., Mangun, G. R., Fries, P., and Friston, K. J. (2012). Canonical microcircuits for predictive coding. Neuron *76*, 695-711.

Beaman, C. B., Eagleman, S. L., and Dragoi, V. (2017). Sensory coding accuracy and perceptual performance are improved during the desynchronized cortical state. Nature Communications *8*: 1308. doi: 10.1038/s41467-017-01030-4

Bekinschtein, T. A., Dehaene, S., Rohaut, B., Tadel, F., Cohen, L., and Naccache, L. (2009). Neural signature of the conscious processing of auditory regularities. Proceedings of the National Academy of Sciences *106*, 1672-1677.

Brainard, D. H., and Vision, S. (1997). The psychophysics toolbox. Spatial Vision *10*, 433-436.

Buzsaki, G., Anastassiou, C.A., and Koch, C. (2012). The origin of extracellular fields and currents—EEG, ECoG, LFP and spikes. Nature Reviews Neuroscience *13*, 407–420.

Chao, Z. C., Takaura, K., Wang, L., Fujii, N., and Dehaene, S. (2018). Large-scale cortical networks for hierarchical prediction and prediction error in the primate brain. Neuron *100*, 1252-1266.

Chaudhuri, R., He, B. J., and Wang, X.-J. (2017). Random recurrent networks near criticality capture the broadband power distribution of human ECoG dynamics. Cerebral Cortex *28*, 3610–3622.

Chennu, S., Noreika, V., Gueorguiev, D., Blenkmann, A., Kochen, S., Ibáñez, A., Owen, A. M., and Bekinschtein, T. A. (2013). Expectation and attention in hierarchical auditory prediction. Journal of Neuroscience *33*, 11194-11205.

Chennu, S., Noreika, V., Gueorguiev, D., Shtyrov, Y., Bekinschtein, T. A., and Henson, R. (2016). Silent expectations: dynamic causal modeling of cortical prediction and attention to sounds that weren't. Journal of Neuroscience *36*, 8305-8316.

Choi, J. W., Lee, J. K., Ko, D., Lee, G. T., Jung, K. Y., and Kim, K. H. (2013). Fronto-temporal interactions in the theta-band during auditory deviant processing. Neuroscience Letters *548*, 120-125.

Clark, A. (2013). Whatever next? Predictive brains, situated agents, and the future of cognitive science. Behavioral and Brain Sciences *36*, 181-204.

Cole, S.R., and Voytek, B. (2017). Brain oscillations and the importance of waveform shape. Trends in Cognitive Sciences *21*, 137–149.

Cowan, N., Winkler, I., Teder, W., and Näätänen, R. (1993). Memory prerequisites of mismatch negativity in the auditory event-related potential (ERP). Journal of Experimental Psychology: Learning, Memory, and Cognition *19*, 909-921.

Crone, N. E., Korzeniewska, A., and Franaszczuk, P. J. (2011). Cortical gamma responses: searching high and low. *Int. J. Psychophysiol. 79*, 9–15.

de Cheveigné, A., Nelken, I. (2017). Filters: When, Why, and How (Not) to Use Them. Neuron *102*, 280-293.

Edwards, E., Soltani, M., Deouell, L. Y., Berger, M. S., and Knight, R. T. (2005). High gamma activity in response to deviant auditory stimuli recorded directly from human cortex. Journal of Neurophysiology *94*, 4269-4280.

Eliades, S. J., Crone, N. E., Anderson, W. S., Ramadoss, D., Lenz, F. A., and Boatman-Reich, D. (2014). Adaptation of high-gamma responses in human auditory association cortex. Journal of Neurophysiology *112*, 2147-2163.

Fahrenfort, J. J., Van Driel, J., Van Gaal, S., and Olivers, C. N. (2018). From ERPs to MVPA using the Amsterdam decoding and modeling toolbox (ADAM). Frontiers in Neuroscience *12*: 368. doi: 10.3389/fnins.2018.00368

Fayyaz, Z., Bahadorian, M., Doostmohammadi, J., Davoodnia, V., Khodadadian, S., and Lashgari, R. (2019). Multifractal detrended fluctuation analysis of continuous neural time series in primate visual cortex. Journal of Neuroscience Methods *312*, 84-92.

Feder, J. (1988). *Fractals.* 4th edn. New York: Springer Science & Business Media.

Fetterhoff, D., Opris, I., Simpson, S.L., Deadwyler, S.A., Hampson, R.E., and Kraft, R.A. (2015). Multifractal analysis of information processing in hippocampal neural ensembles during working memory under Δ_9-tetrahydrocannabinol administration. Journal of Neuroscience Methods *244*, 136–153.

Freeman, W. J. (2004). Origin, structure, and role of background EEG activity. Part 1. Analytic amplitude. *Clin. Neurophysiol. 115*, 2077–2088.

Freeman, W. J., Kozma, R., and Werbos, P. J. (2001). Biocomplexity: adaptive behavior in complex stochastic dynamical systems. Biosystems 59, 109–123.

Freeman, W. J. and Vitiello, G. (2006). Nonlinear brain dynamics as macroscopic manifestation of underlying many-body field dynamics. Physics of Life Reviews *3*, 93–118.

Freeman, W. J., and Zhai, J. (2009). Simulated power spectral density (PSD) of background electrocorticogram (ECoG). Cognitive Neurodynamics *3*, 97-103.

Friston, K.J. (1997). Transients, metastability, and neuronal dynamics. Neuroimage *5*, 164–171.

Friston, K. J. (2000). The labile brain. I. Neuronal transients and nonlinear coupling. Philosophical Transactions of the Royal Society of London. Series B: Biological Sciences *355*, 215-236.

Friston, K., and Kiebel, S. (2009). Predictive coding under the free-energy principle. Philosophical Transactions of the Royal Society B: Biological Sciences *364*, 1211-1221.

Fuentemilla, L. L., Marco-Pallarés, J., Münte, T. F., and Grau, C. (2008). Theta EEG oscillatory activity and auditory change detection. Brain Research *1220*, 93-101.

Garrido, M. I., Friston, K. J., Kiebel, S. J., Stephan, K. E., Baldeweg, T., and Kilner, J. M. (2008). The functional anatomy of the MMN: a DCM study of the roving paradigm. Neuroimage *42*, 936-944.

Gasser, T., Ziegler, P., and Gattaz, W. F. (1992). The deleterious effect of ocular artefacts on the quantitative EEG, and a remedy. European Archives of Psychiatry and Clinical Neuroscience *241*, 352-356.

Gierałtowski, J., Żebrowski, J. J., and Baranowski, R. (2012). Multiscale multifractal analysis of heart rate variability recordings with a large number of occurrences of arrhythmia. Physical Review E *85*: 021915. doi: 10.1103/physreve.85.021915

Gifani, P., Rabiee, H. R., Hashemi, M. H., Taslimi, P., and Ghanbari, M. (2007). Optimal fractal-scaling analysis of human EEG dynamic for depth of anesthesia quantification. Journal of the Franklin Institute *344*, 212-229.

Goldberger, A. L., Amaral, L. A., Glass, L., Hausdorff, J. M., Ivanov, P. C., Mark, R. G., Mietus, J.E., Moody, G.B., Peng, C.-K., and Stanley, H. E. (2000). PhysioBank, PhysioToolkit, and PhysioNet: components of a new research resource for complex physiologic signals. *Circulation 101*, e215-e220.

Grigolini, P., Aquino, G., Bologna, M., Luković, M., and West, B. J. (2009). A theory of 1/f noise in human cognition. Physica A: Statistical Mechanics and its Applications *388*, 4192-4204.

Haenschel, C., Baldeweg, T., Croft, R. J., Whittington, M., and Gruzelier, J. (2000). Gamma and beta frequency oscillations in response to novel auditory stimuli: a comparison of human electroencephalogram (EEG) data with in vitro models. Proceedings of the National Academy of Sciences *97*, 7645-7650.

Haenschel, C., Vernon, D. J., Dwivedi, P., Gruzelier, J. H., and Baldeweg, T. (2005). Event-related brain potential correlates of human auditory sensory memory-trace formation. Journal of Neuroscience *25*, 10494-10501.

Halgren, E., Baudena, P., Clarke, J. M., Heit, G., Liégeois, C., Chauvel, P., and Musolino, A. (1995). Intracerebral potentials to rare target and distractor auditory and visual stimuli. I. Superior temporal plane and parietal lobe. Electroencephalography and Clinical Neurophysiology *94*, 191-220.

Halsey, T. C., Jensen, M. H., Kadanoff, L. P., Procaccia, I., and Shraiman, B. I. (1986). Fractal measures and their singularities: The characterization of strange sets. Physical Review A *33*: 1141.

doi: 10.1103/PhysRevA.33.1141.

He, B. J., Zempel, J. M., Snyder, A. Z., and Raichle, M. E. (2010). The temporal structures and functional significance of scale-free brain activity. Neuron *66*, 353-369.

He, B. J. (2014). Scale-free brain activity: past, present, and future. *Trends in Cognitive Sciences 18*, 480-487.

Hermes, D., Miller, K. J., Wandell, B. A., and Winawer, J. (2014). Stimulus dependence of gamma oscillations in human visual cortex. Cerebral Cortex *25*, 2951-2959.

Hermes, D., Nguyen, M., and Winawer, J. (2017). Neuronal synchrony and the relation between the blood-oxygen-level dependent response and the local field potential. PLoS Biology *15*: e2001461. doi: 10.1371/journal.pbio.2001461

Hermes, D., Petridou, N., Kay, K., and Winawer, J. (2019). An image-computable model for the stimulus selectivity of gamma oscillations. bioRxiv *583567*. doi: 10.1101/583567

Hikishima, K., Quallo, M. M., Komaki, Y., Yamada, M., Kawai, K., Momoshima, S., Okano, H.J., Sasaki, E., Tamaoki, N., Lemon, R.N., Iriki, A., and Okano, H. (2011). Population-averaged standard template brain atlas for the common marmoset (Callithrix jacchus). Neuroimage *54*, 2741-2749.

Hsiao, F. J., Wu, Z. A., Ho, L. T., and Lin, Y. Y. (2009). Theta oscillation during auditory change detection: an MEG study. Biological Psychology *81*, 58-66.

Hu, K., Ivanov, P. C., Chen, Z., Carpena, P., and Stanley, H. E. (2001). Effect of trends on detrended fluctuation analysis. Physical Review E *64*, 011114. doi: 10.1103/PhysRevE.64.011114

Hurst, H. E. (1951). Long-term storage capacity of reservoirs. Transactions of the American Society of Civil Engineers *116*, 770-799.

Lakatos, P., Musacchia, G., O'Connel, M.N., Falchier, A.Y., Javitt, D.C., and Schroeder, C.E. (2013). The spectrotemporal filter mechanism of auditory selective attention. Neuron *77*, 750–761.

Lopes da Silva, F. (2013). EEG and MEG: relevance to neuroscience. Neuron *80*, 1112–1128.

Ihlen, E. A. F. (2012). Introduction to multifractal detrended fluctuation analysis in Matlab. Frontiers in Physiology *3*, 141. doi: 10.3389/fphys.2012.00141

Jamovi project (2019). *jamovi* (Version 0.9) [Computer Software]. Retrieved from https://www.jamovi.org

Javitt, D. C., Schroeder, C. E., Steinschneider, M., Arezzo, J. C., and Vaughan Jr, H. G. (1992). Demonstration of mismatch negativity in the monkey. Electroencephalography and Clinical Neurophysiology *83*, 87-90.

Kantelhardt, J. W., Zschiegner, S. A., Koscielny-Bunde, E., Havlin, S., Bunde, A., and Stanley, H. E. (2002). Multifractal detrended fluctuation analysis of nonstationary time series. Physica A: Statistical Mechanics and its Applications *316*, 87-114.

Kantelhardt, J. W. (2011). Fractal and multifractal time series. In Mathematics of Complexity and Dynamical Systems (ed. R.A. Meyers), pp. 463–487. New York, NY: Springer.

Kelso, J.A.S. (1995). Dynamic patterns: the self-organization of brain and behavior. MIT Press, Cambridge, Mass.

Ko, D., Kwon, S., Lee, G. T., Im, C. H., Kim, K. H., and Jung, K. Y. (2012). Theta oscillation related to the auditory discrimination process in mismatch negativity: oddball versus control paradigm. Journal of Clinical Neurology *8*, 35-42.

Komatsu, M., Takaura, K., and Fujii, N. (2015). Mismatch negativity in common marmosets: Whole-cortical recordings with multi-channel electrocorticograms. Nature Scientific Reports *5*, 15006. doi: 10.1038/srep15006

Komatsu, M., Sugano, E., Tomita, H., and Fujii, N. (2017). A chronically implantable bidirectional neural interface for non-human primates. Frontiers in Neuroscience *11*, 514. doi: 10.3389/fnins.2017.00514

Lakatos, P., Shah, A. S., Knuth, K. H., Ulbert, I., Karmos, G., and Schroeder, C. E. (2005). An oscillatory hierarchy controlling neuronal excitability and stimulus processing in the auditory cortex. Journal of Neurophysiology *94*, 1904-1911.

Lumaca, M., Trusbak Haumann, N., Brattico, E., Grube, M., and Vuust, P. (2019). Weighting of neural prediction error by rhythmic complexity: A predictive coding account using mismatch negativity. European Journal of Neuroscience *49*, 1597-1609.

Ma, Q., Ning, X., Wang, J., and Bian, C. (2006). A new measure to characterize multifractality of sleep electroencephalogram. Chinese Science Bulletin *51*, 3059-3064.

MacLean, S. E., and Ward, L. M. (2014). Temporo-frontal phase synchronization supports hierarchical network for mismatch negativity. Clinical Neurophysiology *125*, 1604-1617.

Mandelbrot, B. B. (2003). Multifractal power law distributions: Negative and critical dimensions and other “anomalies,” explained by a simple example. Journal of Statistical Physics *110*, 739-774.

Manning, J. R., Jacobs, J., Fried, I., and Kahana, M. J. (2009). Broadband shifts in local field potential power spectra are correlated with single-neuron spiking in humans. Journal of Neuroscience *29*, 13613-13620.

Marshall, L., Mölle, M., and Bartsch, P. (1996). Event-related gamma band activity during passive and active oddball tasks. Neuroreport *7*, 1517-1520.

Miller, K. J., Leuthardt, E. C., Schalk, G., Rao, R. P., Anderson, N. R., Moran, D. W., Miller, J.W., and Ojemann, J. G. (2007). Spectral changes in cortical surface potentials during motor movement. Journal of Neuroscience *27*, 2424-2432.

Miller, K. J., Sorensen, L. B., Ojemann, J. G., and Den Nijs, M. (2009a). Power-law scaling in the brain surface electric potential. PloS Computational Biology *5*, e1000609. doi: 10.1371/journal.pcbi.1000609

Miller, K. J., Zanos, S., Fetz, E. E., Den Nijs, M., and Ojemann, J. G. (2009b). Decoupling the cortical power spectrum reveals real-time representation of individual finger movements in humans. Journal of Neuroscience *29*, 3132-3137.

Miller, K. J. (2010). Broadband spectral change: evidence for a macroscale correlate of population firing rate? Journal of Neuroscience *30*, 6477-6479.

Miller, K. J., Hermes, D., Pestilli, F., Wig, G. S., and Ojemann, J. G. (2017). Face percept formation in human ventral temporal cortex. Journal of Neurophysiology *118*, 2614-2627.

Mukamel, R., Gelbard, H., Arieli, A., Hasson, U., Fried, I., and Malach, R. (2005). Coupling between neuronal firing, field potentials, and FMRI in human auditory cortex. Science *309*, 951-954.

Nagasaka, Y., Shimoda, K., and Fujii, N. (2011). Multidimensional recording (MDR) and data sharing: an ecological open research and educational platform for neuroscience. *PloS One*, *6*, e22561. doi: 10.1371/journal.pone.0022561

Nagy, Z., Mukli, P., Herman, P., and Eke, A. (2017). Decomposing multifractal crossovers. Frontiers in Physiology *8*, 533. doi: 10.3389/fphys.2017.00533

Näätänen, R., Gaillard, A. W., and Mäntysalo, S. (1978). Early selective-attention effect on evoked potential reinterpreted. Acta Psychologica *42*, 313-329.

Näätänen, R., Paavilainen, P., Rinne, T., and Alho, K. (2007). The mismatch negativity (MMN) in basic research of central auditory processing: a review. Clinical Neurophysiology *118*, 2544-2590.

Nieto-Diego, J., and Malmierca, M. S. (2016). Topographic distribution of stimulus-specific adaptation across auditory cortical fields in the anesthetized rat. PLoS Biology *14*, e1002397. doi: 10.1371/journal.pbio.1002397

Noreika, V., Canales-Johnson, A., Johnson, A., Arnatkevičiūtė, A., Koh, J., Chennu, S., and Bekinschtein, T. A. (2019a). Wakefulness state modulates conscious access: Suppression of auditory detection in the transition to sleep. bioRxiv *155705*. doi: 10.1101/155705

Noreika, V., Kamke, M. R., Canales-Johnson, A., Chennu, S., Bekinschtein, T. A., and Mattingley, J. B. (2019b). Alertness fluctuations during task performance modulate cortical evoked responses to transcranial magnetic stimulation. bioRxiv *155754*. doi: 10.1101/155754

Paluš, M. (1996). Nonlinearity in normal human EEG: cycles, temporal asymmetry, nonstationarity and randomness, not chaos. Biological Cybernetics *75*, 389-396.

Papo, D. (2014). Functional significance of complex fluctuations in brain activity: from resting state to cognitive neuroscience. Frontiers in Systems Neuroscience *8*, 112. doi: 10.3389/fnsys.2014.00112

Parras, G. G., Nieto-Diego, J., Carbajal, G. V., Valdés-Baizabal, C., Escera, C., and Malmierca, M. S. (2017). Neurons along the auditory pathway exhibit a hierarchical organization of prediction error. Nature Communications *8*, 2148. doi: 10.1038/s41467-017-02038-6

Pelli, D. G. (1997). The VideoToolbox software for visual psychophysics: Transforming numbers into movies. Spatial Vision *10*, 437-442.

Peng, C. K., Havlin, S., Stanley, H. E., and Goldberger, A. L. (1995). Quantification of scaling exponents and crossover phenomena in nonstationary heartbeat time series. Chaos: An Interdisciplinary Journal of Nonlinear Science *5*, 82-87.

Pérez- González, D., Malmierca, M. S., and Covey, E. (2005). Novelty detector neurons in the mammalian auditory midbrain. European Journal of Neuroscience *22*, 2879-2885.

Rasch, M. J., Gretton, A., Murayama, Y., Maass, W., and Logothetis, N. K. (2008). Inferring spike trains from local field potentials. Journal of Neurophysiology *99*, 1461-1476.

Renart, A., De La Rocha, J., Bartho, P., Hollender, L., Parga, N., Reyes, A., and Harris, K. D. (2010). The asynchronous state in cortical circuits. Science *327*, 587-590.

Riedi, R. H. (1999) Multifractal processes. In Long Range Dependence: Theory and Applications (Eds. P. Doukhan, M. S. Taqqu, and G. Oppenheim), pp 625-715. Birkhäuser.

Rorden, C., Karnath, H. O., and Bonilha, L. (2007). Improving lesion-symptom mapping. Journal of Cognitive Neuroscience *19*, 1081-1088.

Rubin, J., Ulanovsky, N., Nelken, I., and Tishby, N. (2016). The representation of prediction error in auditory cortex. PLoS Computational Biology *12*, e1005058. doi: 10.1371/journal.pcbi.1005058

Schroeder, C. E., and Lakatos, P. (2009). The gamma oscillation: master or slave? Brain Topography *22*, 24-26.

Schroeder, C.E., and Lakatos, P. (2009). Low-frequency neuronal oscillations as instruments of sensory selection. Trends in Neurosciences *32*, 9–18.

Solomon, S. G., and Kohn, A. (2014). Moving sensory adaptation beyond suppressive effects in single neurons. Current Biology *24*, R1012-R1022.

Theiler, J. (1990). Estimating fractal dimension. Journal of the Optical Society of America A 7, 1055-1073.

Tognoli, E., and Kelso, J.A.S. (2014). The metastable brain. Neuron *81*, 35–48.

Ulanovsky, N., Las, L., and Nelken, I. (2003). Processing of low-probability sounds by cortical neurons. Nature Neuroscience *6*, 391-398.

Ulanovsky, N., Las, L., Farkas, D., and Nelken, I. (2004). Multiple time scales of adaptation in auditory cortex neurons. Journal of Neuroscience *24*, 10440-10453.

van de Velde, M., van Erp, G., and Cluitmans, P. J. (1998). Detection of muscle artefact in the normal human awake EEG. Electroencephalography and Clinical Neurophysiology *107*, 149-158.

Weiss, B., Clemens, Z., Bódizs, R., Vágó, Z., and Halász, P. (2009). Spatio-temporal analysis of monofractal and multifractal properties of the human sleep EEG. Journal of Neuroscience Methods *185*, 116-124.

Whitmire, C. J. and Stanley, G. B. (2016). Rapid sensory adaptation redux: A circuit perspective. Neuron 92, 298–315.

Zerlaut, Y. and Destexhe, A. (2017. Enhanced responsiveness and low-level awareness in stochastic network states. Neuron *94*, 1002–1009.